ELSEVIER

Ultrasound in Med. & Biol., Vol. 22, No. 2, pp. 261–270, 1996

0301-5629/96 $15.00 + .00

0301-5629(95)02031-4

●*Original Contribution*

AMPLITUDE, ISOBAR AND GREY-SCALE IMAGING OF ULTRASONIC SHADOWS BEHIND RIGID, ELASTIC AND GASEOUS SPHERES

L. FILIPCZYŃSKI, T. KUJAWSKA, R. TYMKIEWICZ and J. WÓJCIK
Department of Ultrasonics, Institute of Fundamental Technological Research,
Polish Academy of Sciences, Warsaw, Poland

(*Received* 12 *January* 1995; *in final form* 25 *July* 1995)

Abstract—The theory of wave reflection from spherical obstacles was applied for determination of the cause of the shadow created by plane wave pulses incident on rigid, steel, gaseous spheres and on spheres made of kidney stones. The spheres were immersed in water which was assumed to be a tissuelike medium. Acoustic pressure distributions behind the spheres with the radii of 1 mm, 2.5 mm and 3.5 mm were determined at the frequency of 5 MHz. The use of the exact wave theory enabled us to take into account the diffraction effects. The computed pressure distributions were verified experimentally at the frequency of 5 MHz for a steel sphere with a 2.5-mm radius. The experimental and theoretical pulses were composed of about three ultrasonic frequency periods. Acoustic pressure distributions in the shadow zone of all spheres were shown in the amplitude axonometric projection, in the grey scale and also as acoustic isobar patterns. Our analysis confirmed existing simpler descriptions of the shadow from the point of view of reflection and refraction effects; however, our approach is more general, also including diffraction effects and assuming the pulse mode. The analysis has shown that gaseous spherical inclusions caused shadows with very high dynamics of acoustic pressures that were about 15 dB higher in relation to all the other spheres. The shadow length, determined as the length at which one observes a 6-dB drop of the acoustic pressure, followed the relation $r_{-6dB} = 3.7a^2/\lambda$ with the accuracy of about 20% independent of the sphere type. λ denotes the wavelength and a the sphere radius. Thus, a theoretical possibility of differentiating between gaseous and other inclusions and of estimation of the inclusion size in the millimeter range from the shadow was shown. The influence of the frequency-dependent attenuation on the shadow will be considered in the next study.

Key Words: **Shadow, Pulses, Spheres, Ultrasonography.**

INTRODUCTION

The shadow that occurs in ultrasonography behind various pathological structures like cancerous tissue, cysts, calcifications, gas bubbles and so forth contains information about the detected structure. However, the existing theory, based on geometric acoustics, does not allow the nature of the detected structure to be identified.

The purpose of this article is to find a numerical description of the ultrasonic shadow produced under the plane-wave condition assuming that the shadowing structure is in the form of a sphere with various acoustic parameters different from those of the surrounding, tissuelike medium. Next, we explore the usefulness of this information to the diagnostic ultrasonic examination.

Until now one can find in the literature only studies describing the shadow produced by structures in an ultrasonic field from the point of view of geometrical (ray) acoustics. In such cases, the ratio of the structure dimension to the wavelength, which is important for its detection and for diffraction effects, is completely ignored. Moreover, all the existing reports assume that the shadowing structures are in the form of a circular cylinder, which is convenient for explaining the refraction phenomena (see, *e.g.*, Robinson et al. 1981; Soetano and Reid 1991; Ziskin et al. 1990). However, they do not occur in the majority of cases in clinical ultrasonography (with the exception of blood vessels). Another limitation is caused by considering the continuous radiation mode while, in reality, short pulses are used.

Address correspondence to: L. Filipczyński, Department of Ultrasonics, Institute of Fundamental Technological Research, Polish Academy of Sciences, 00-049 Warsaw, Poland.

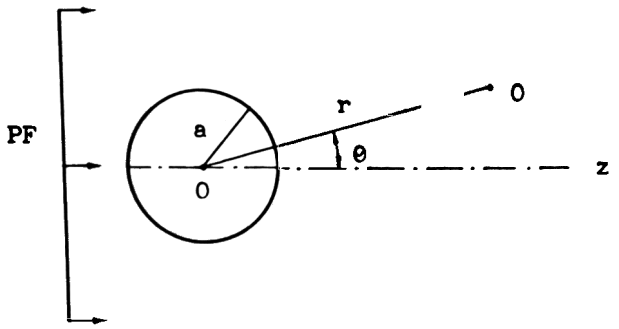

Fig. 1. Coordinate system used: r—radius (distance from the sphere center 0), θ—azimuth, z—symmetry axis, a—sphere radius, PF—front of the incident plane wave, 0′—observation point.

In our study, we investigate small pathological structures in their first stage of development, which are of greatest importance for the early diagnosis of pathological processes. Therefore, we have chosen structures of spherical shape with small radii of 1 mm, 2.5 mm, and 3.5 mm. In such cases, diffraction effects are the determinant for the shadow formation and they cannot be described by geometrical (ray) acoustics. Only the wave acoustics applied in this article are responsible for the exact description of the shadowing effects. Consequently, the corresponding mathematical equations were applied and considerable numerical computations were carried out to visualize the shadow in various presentation modes.

Such a treatment was applied by the first two authors to investigate shadows in the case of continuous waves (Filipczyński and Kujawska 1989; Filipczyński et al. 1991). The problem will now be investigated from the point of view of ultrasonography where extremely short pulses are applied.

Water was chosen as a tissuelike medium for the following reasons. First, densities and wave speeds of water and soft tissues are similar (attenuation is entirely different). However, we wanted first to simplify, as much as possible, the complicated phenomenon of the shadow formation by neglecting the frequency-dependent attenuation. Second, water enabled us to measure pressure distributions in the shadow range point-by-point to verify the derived theoretical and numerical procedures. The influence of attenuation on the shadow formation will be analysed in the next stage of this study.

FUNDAMENTAL RELATIONS

The shadow behind a sphere can be determined from expressions describing the acoustic pressure, p_s, emerging around the sphere. It is the sum of acoustic pressures of the plane wave p_i incident on the sphere and of the wave p_r reflected (or scattered) from the sphere (Morse and Ingard 1968)

$$p_s = p_i + p_r \tag{1}$$

The acoustic pressure of the wave reflected from the sphere is obtained as the solution of the scalar wave equation in the medium surrounding the sphere for boundary conditions corresponding to the sphere material.

The monochromatic plane pressure wave incident on the sphere (Fig. 1) is (Hasegawa et al. 1977; Rudgers 1969):

$$\begin{aligned} p_i(t) &= p_o \exp[j\omega(t - r\cos\theta/c)] \\ &= p_o \exp[jka(ct - r\cos\theta)/a] \\ &= p_o \exp(jka\tau') \end{aligned}$$

The wave reflected from the sphere can be presented in the form:

$$\begin{aligned} p_r(t) &= p_o(a/2r) f_f(ka) \exp[j\omega(t - r/c)] \\ &= p_o(a/2r) f_f(ka) \exp[jka\tau \end{aligned}$$

In Eqns (2) and (3), describing the incident and

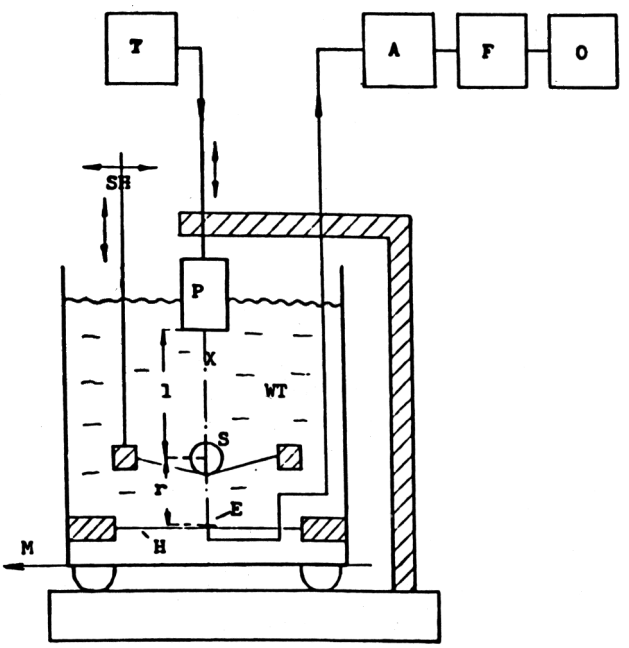

Fig. 2. Principle of the measurement system: T—transmitter, P—ultrasonic probe, S—sphere, H—membrane of the PVDF hydrophone, E—hydrophone's electrode, A—wide-band amplifier (28 dB), F—low pass filter 29 MHz, O—oscilloscope LeCroy 945A, M—microscope table, SH—sphere holder, WT—water tank, X—axis of the ultrasonic beam.

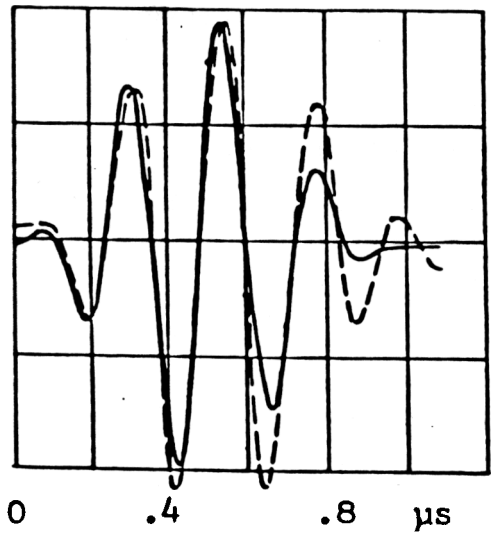

Fig. 3. Shape of the ultrasonic pulse used in calculations (solid line) and applied in measurements (dashed line).

the reflected waves, dimensionless time coordinates τ and τ were introduced, respectively (Rudgers 1969) They are equal to:

$$\tau' = (ct - r\cos\theta)/a \quad \text{and}$$

$$\tau = (ct - r)/a \quad (4a,b)$$

hence, one obtains the relation

$$\tau = \tau' + (\cos\theta - \ )r/a \qquad (5)$$

One should notice that $\tau' = \tau$ when $r = 0$ or $\theta = 0$. It means that both waves (incident and reflected) reach the coordinates $r = 0$ and $\theta = 0$ at the same time.

$f_f(ka)$, occurring in Eqn (3), is called the *reflection form function.* It equals (Rudgers 1969):

$$f_f(ka) = -2(kr/ka)\exp(jkr)\sum_{m=0}^{\infty}(2m + \times (-j)^{m+1}\sin\eta_m\exp(j\eta_m)$$

$$h_m^{(2)}(kr)P_m(\cos\theta) \qquad (6)$$

where P_m is the Legendre polynomial, j_m is the spherical Bessel function, $h_m^{(2)}$ is the spherical Hankel function of the second kind, r is the distance from the sphere center and θ is the azimuth (Fig. 1), and:

$$j\sin\eta_m\exp(j\eta_m) = c_m \qquad (7)$$

is a complex number that can be found from boundary conditions on the sphere surface (see Appendix).

Because the system under consideration is assumed to be linear and invariant, there exists in the (dimensionless) frequency domain ka the following relation:

$$S_r(ka) = H(ka)\cdot S_i(ka) \qquad (8)$$

where $S_r(ka)$, $S_i(ka)$ denote spectra of the reflected and incident pulses, and $H(ka)$ is the (spectral) transfer function. It can be found as the response of the system to the unit harmonic signal $\exp(jka\tau)$ (Dieulesaint and Royer 1974). Therefore, one obtains, from Eqn (3):

$$H(ka) = (a/2r)f_f(ka) \qquad (9)$$

It means that every monochromatic component of the incident pulse spectrum should be multiplied by the corresponding value of the transfer function in Eqn (9).

The pulse shape of the reflected wave can be expressed by the inverse Fourier transform:

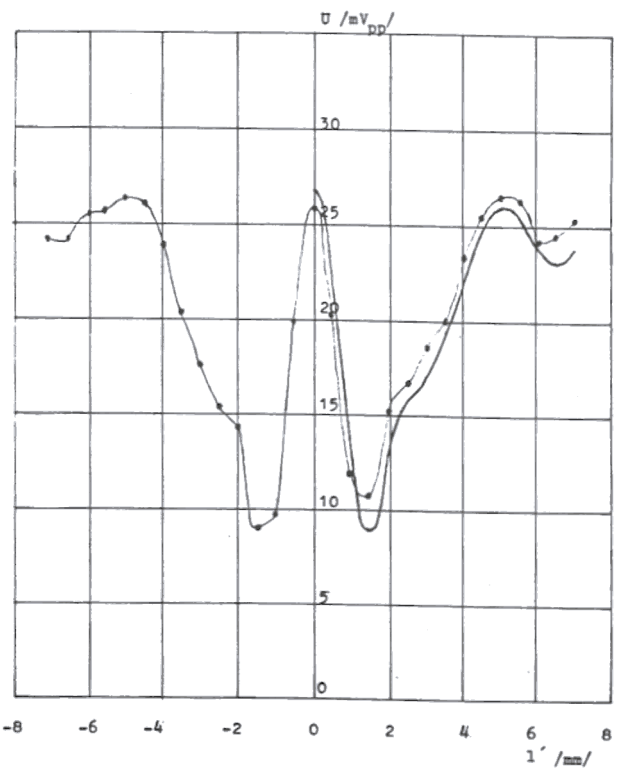

Fig. 4. Measured (thin curve with points) and computed (thick curve) pressure distributions behind the steel sphere (sphere radius $a = 2.5$ mm, $f = 5$ MHz, $ka = 16.7\pi$). Vertical coordinate presents the voltage measured by the hydrophone, horizontal coordinate–off-axis distance. The distance between the sphere center and the electrode equaled 35 mm.

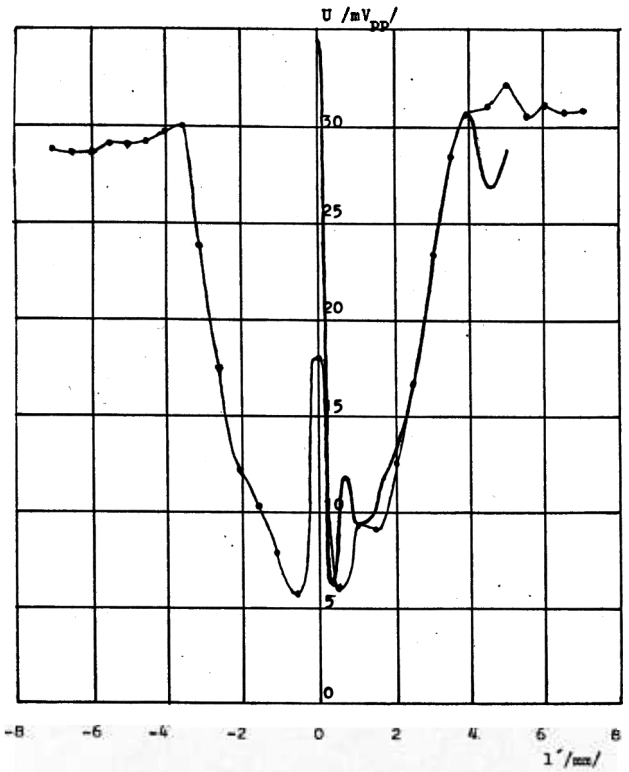

Fig. 5. Same parameters as those in Fig. 4, however, for the small distance between the sphere center and the electrode, $r = 10.8$ mm.

$$p_r(\tau) = (1/2\pi)p_o \int_{-\infty}^{\infty} (a/2r) f_f(ka) S_i(ka) \times \exp(jka\tau) d(ka) \quad (10)$$

where S_i is the spectrum of the incident pulse equal to:

$$S_i(ka) = \int_{-\infty}^{\infty} p_i(\tau') \exp(-jka\tau') d\tau' \quad (11)$$

The interference of the reflected pulse in Eqn (10) with the incident pulse:

$$p_i(\tau') = p_o(1/2\pi) \int_{-\infty}^{\infty} S_i(ka) \exp(jka\tau') d(ka) \quad (12)$$

finally forms the ultrasonic field around the sphere.

It is assumed that the incident ultrasonic pulse with the carrier frequency $f_o = k_o c/2\pi$ has an envelope of the Hanning function.

For the Hanning pulse with b sinusoidal cycles (b = 4) the acoustic pressure of the incident wave equals:

$$p_i(\tau') = \cap(y) \sin k_o a\tau \quad (13)$$

$$\cap(y) = \begin{cases} \cos^2[\pi(\tau'/d - \frac{1}{2})], & \text{when } |y| \le \frac{1}{2} \\ 0 & \text{when } |y| > \frac{1}{2} \end{cases}$$

and:

$$d = 2\pi b/k_o a$$

The spectrum of this pulse:

$$S_i(ka) = (2/p_o) \int_o^d \sin(k_o a\tau') \cos^2[\pi(\tau'/d - \tfrac{1}{2})] \times \exp(-jka\tau') d\tau'$$

can be found by means of indefinite integral tables (Bronsrtejn and Semendjajev 1967).

All the spherical functions were determined up to the order of $m = x + 15$, where x is the argument of the corresponding function; recursion formulae were also used (Rzhevkin, 1960).

MATERIAL OF SPHERES

Four types of sphere material were considered: rigid spheres (r), steel spheres (s), spheres made of kidney stones (k) and gaseous spheres (g). The first and the last ones represent two extreme cases of materials with highest and very low acoustic impedances. The rigid sphere is interesting as a theoretical model and can be relatively simply described mathematically. Also, the interpretation of the wave diffraction is simple since such a sphere is impenetrable for waves. For the same reason the gaseous sphere is of interest. It is also important as a bubble model, because bubbles are frequently observed during ultrasonic examination (in

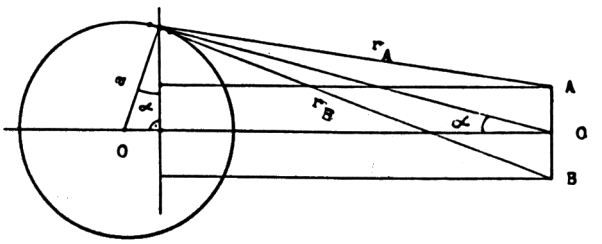

Fig. 6. Geometry of the sphere and the hydrophone's electrode AB. r_A—path length of the diffracted wave reaching the point A, r_B—path length of the diffracted wave reaching the point B. $AB = 2b$—diameter of the electrode, $00' = r$ distance between the electrode and the sphere center.

intestines, in biliary ducts and so forth [Kowalski 1994]).

In the case of rigid spheres, the coefficient, c_m, equals simply (see Appendix):

$$c_m = -j_m'(ka)/h_m^{(2)\prime}(ka) \qquad (16)$$

while, for a gaseous sphere, one obtains (see Appendix)

$$c_m = -j_m(ka)/h_m^{(2)}(ka) \qquad (17)$$

The spheres made of kidney stone material are typical elastic structures with properties between rigid and gaseous spheres. They can also be used to represent calcifications, which are common in the case of neoplastic disease.

Acoustic properties of kidney stones, $c_1 = 3015$ m/s, $\rho c = 4.76 \times 10^6$ kg/m^{2}s ($\rho = 1600$ kg/m^3), were taken from Singh and Agarwal (1990). The value of the Poisson ratio ($\nu = 0.2$) was assumed (as for porcelain and glass). Hence, the transverse wave speed could be determined (Filipczyński et al. 1966):

$$c_2 = c_1[2(1-\nu)/(\ -2\nu)]^{-1/2} = 1840 \text{ m/s} \qquad (18)$$

The coefficient, c_m [see eqn (7)], could now be determined by means of Eqns (A1)–(A7) (see Appendix).

Steel spheres were chosen mainly as their properties are close to rigid spheres and due to their accessibility. Wave speeds and the density used for calculations were: $c_1 = 5900$ m/s, $c_2 = 3260$ m/s and $\rho = 7800$ kg/m^3.

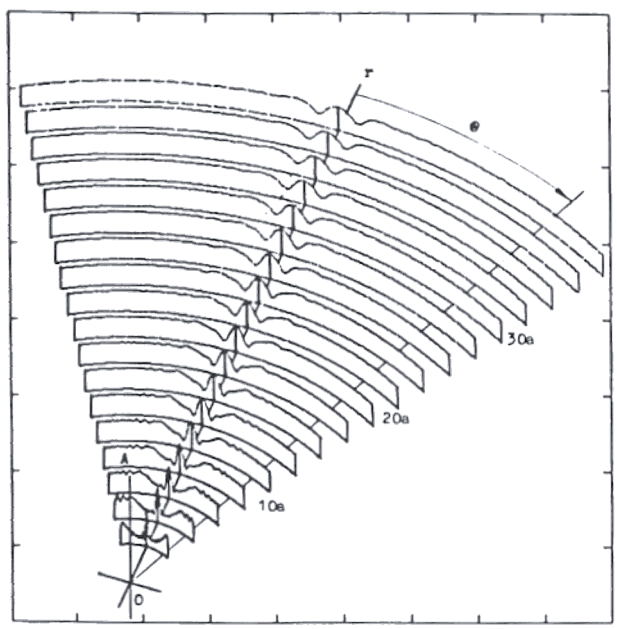

Fig. 7. Computed pressure distributions behind the sphere of the kidney stone 2.5 mm in radius ($f = 5$ MHz, $ka = 16.7\pi$) presented in the axonometric projection r, θ, A. A—pressure amplitude.

EXPERIMENTAL DETERMINATION OF PRESSURE DISTRIBUTIONS

To verify our analysis and its numerical results, measurements were performed in the shadow zone behind a stainless steel sphere 2.5 mm in radius immersed in water, which has tissuelike properties. The sphere was located on the top of a very thin plastic foil (Fig. 2). The ultrasonic incident wave pulse with the frequency of 5 MHz was generated by a transceiving probe (Unipan 5L0 25°C). To approach the conditions typical for ultrasonography, a short electric pulse was generated, resulting in the ultrasonic pulse shown in Fig. 3. It was measured for $l = 51.5$ cm by means of a PVDF membrane hydrophone with an electrode diameter of 0.5 mm. Also in Fig. 3, the theoretical pulse (Hanning pulse) used in the calculations is shown. The two pulses seem to be very similar.

Pressure distributions measured in the incident wave perpendicularly to its propagation direction have shown that the incident wave is locally plane (±0.5 dB) at least in the region of $l' = \pm 4$ mm where l' is the off-axis distance. The measurements of the pressure distribution were carried out in distances $r = 24$–45 mm behind the sphere showing good agreement with theoretical curves (Fig. 4). The distributions obtained have an axial symmetry with a main maximum (main lobe) on the beam axis. Then they show two valleys situated symmetrically.

Only at smaller distances, r, one obtains a disagreement in the value of the main lobe amplitude (Fig. 5). This can be explained by the fact that the hydrophone's electrode diameter (0.5 mm) is too large for smaller distances, r. It can be easily shown that in such a case one obtains the averaging effect on the electrode due to its finite size. Assuming that the difference between the extreme path lengths of the diffracted wave (Fig. 6) should be $\epsilon\lambda = (\frac{1}{8})\lambda$ one obtains, for the maximum electrode radius at the distance of $r = 4a$, the value (Beissner 1985):

$$b = (\epsilon\lambda/2)\{r^2[a^2 - (\epsilon\lambda/s)^2]^{-1} + 1\}^{1/2} = 0.08 \text{ mm} \qquad (19)$$

This means that, in this case, the electrode diameter should be about three times smaller than the one used in our hydrophone. Thus, one can finally conclude that our theoretical results were confirmed by measurements.

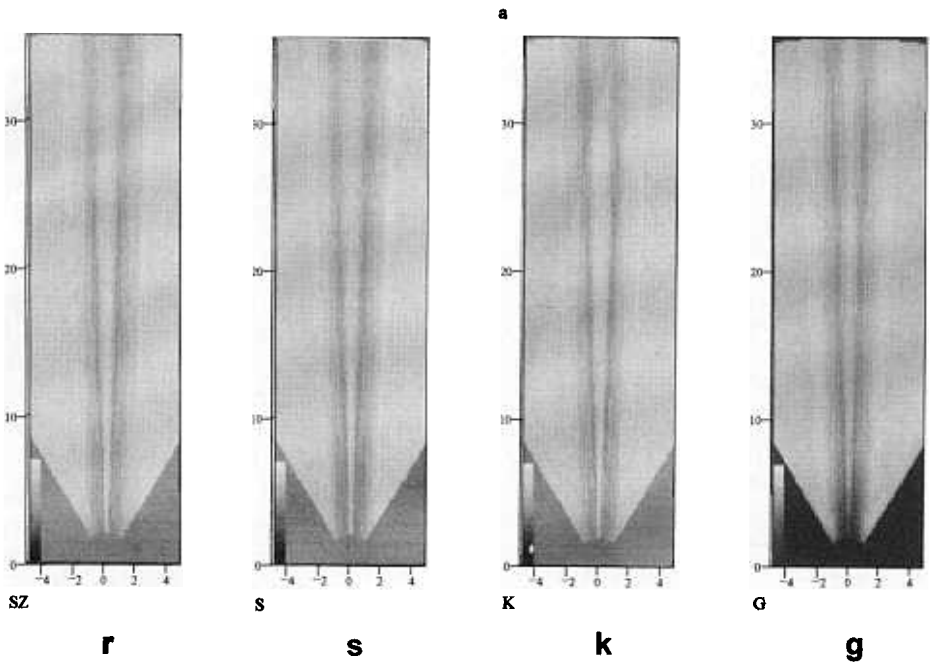

Fig. 8. Computed grey-scale shadow images behind spheres with radius a = 2.5 mm (f = 5 MHz, ka = 16.7π). r—rigid sphere, s—steel sphere, k—kidney stone sphere, g—gaseous sphere.

PRESSURE AMPLITUDE DISTRIBUTIONS BEHIND THE SPHERE

A demonstrative image of pressure amplitudes behind the sphere was obtained in axonometric projection in the coordinate system r, θ, A, where A denotes the pressure amplitude. It shows distinctly that the shadow formation is an interference process. Figure 7 presents as an example the computed distributions behind a sphere, 2.5 mm in radius, made of the kidney stone. It shows high peaks (pressure maxima) on the beam axis (for $\theta = 0$). Near the sphere, some of them are even higher than the level of the incident wave (assumed to be 1). However, the peaks change their shapes by becoming flatter and diminishing with distance. The two valleys (pressure minima) located symmetrically on both sides of the beam axis represent the main shadowing effect. One can also observe the succeeding maxima and minima when increasing the angle θ. However, they are much smaller and diminish with angle θ. Their contribution to the shadow effect is much smaller although clearly visible in the grey-scale images.

Maximum pressures occurring on the shadow beam axis ($\theta = 0$) are, in some cases, higher than the amplitude of the incident wave. This may be caused by waves diffracted around the sphere and meeting with the same phase on the symmetry axis z behind the sphere. A similar effect was observed in optics (Filipczyński et al. 1991). Minima of pressures occur

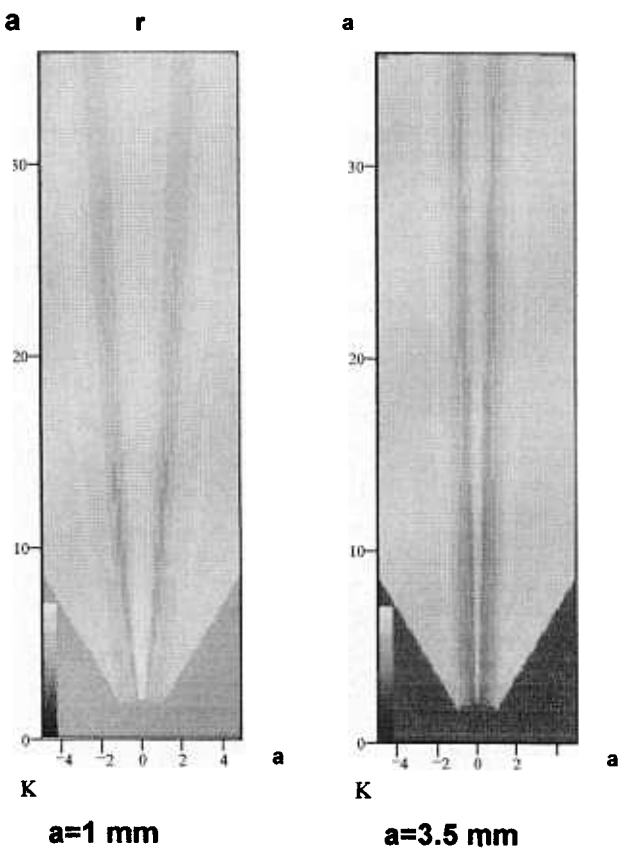

Fig. 9. Computed grey-scale shadow images behind spheres made of kidney stone with the radius of 1 mm and 3.5 mm (f = 5 MHz, ka = 6.67π and 23.3., respectively).

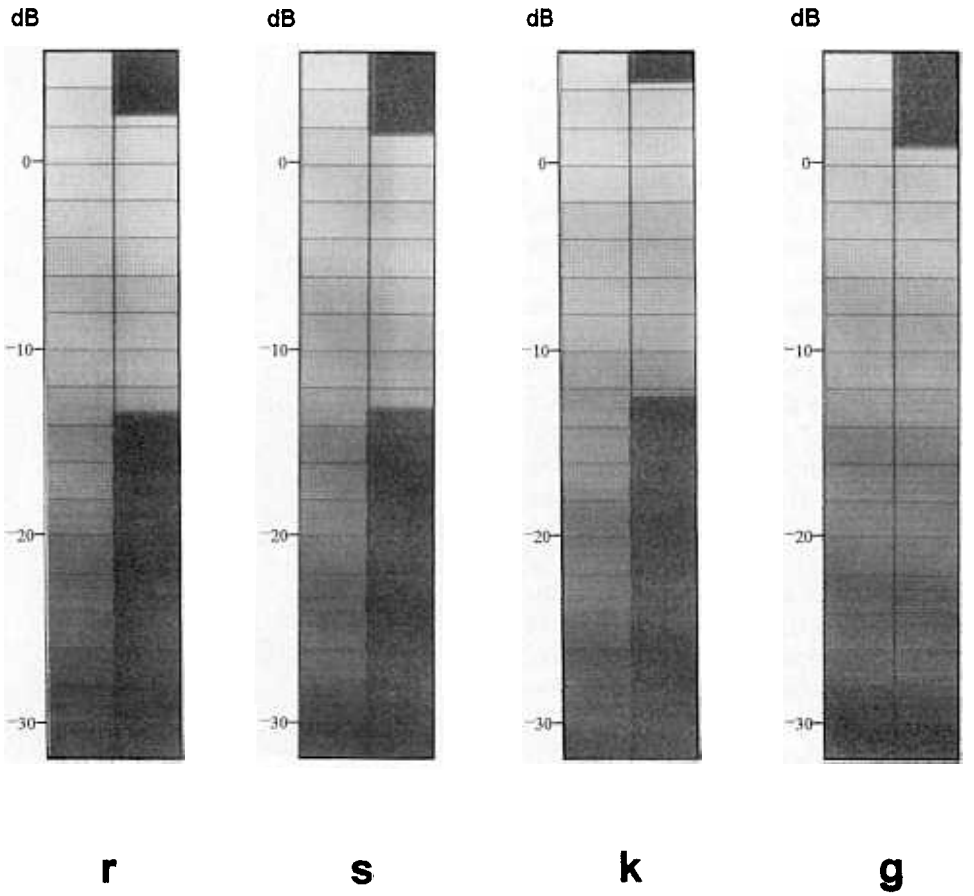

Fig. 10. Dynamics of acoustic pressures represented in grey-scale shadow images of Fig. 8.

near the symmetry axis at the places where the diffracted waves are overlapping with opposite phases.

SHADOW OF THE SPHERE IN THE GREY SCALE

The shadow in ultrasonography is usually presented as a two-dimensional image in angular (r, θ) or rectangular (x, y) coordinates. It is vizualized on the monitor screen due to scattering of the ultrasonic beam on tissue inhomogeneities which form a bright background. In this way, higher acoustic pressures generate brighter points while lower pressures indicate the shadow.

Table 1. Dynamics of acoustic pressures occurring in shadow beams for various spheres (in decibels).

	a =			Dynamics	
Type of sphere	1 mm	2.5 mm	3.5 mm	Mean	SD
	13	16	22	17.0	2.8
	12.5	15	18	15.2	2.8
	13	17	19	16.3	3.0
	25	32	38	31.7	6.5

The brightness dynamics of monitor screens allows for values up to 40 dB, therefore, it is necessary to use lin–log amplifiers to compress various tissue echoes, even those reaching dynamics values equal to 100 dB.

Computed pressure distributions were imaged in the grey scale, representing the dynamics of 38 dB composed of 2-dB steps. Zero level corresponded to the incident wave pressure (with the amplitude equal to 1). Since the pressure amplitudes on the symmetry axis behind the sphere were sometimes higher than 1 the maximum grey-scale level of +6 dB was chosen.

The pressure field was determined for the distance, r, in the range from $2a$ to $36a$ (in $2a$ steps) and for the angle $\theta = \pm 30°$ (in 0.2° steps). A transformation of the polar into rectangular coordinates and a linear interpolation were carried out when performing the shadow beam patterns.

Fig. 8 presents as an example grey-scale shadow image of pressure distributions computed behind rigid, steel, kidney stone, and gaseous spheres. The sphere

radius in all the cases was equal to $a = 2.5$ mm ($f = 5$ MHz, $ka = 16.7\pi$).

Similar grey-scale images of pressure distributions were obtained for spheres of the same materials, however, with the radius equal to 1 mm and 3.5 mm ($f = 5$ MHz, $ka = 6.67\pi$ and 23.3π, respectively).

Figure 9 shows an example the grey-scale shadow images of kidney stone spheres with radii of 1 mm and 3.5 mm.

Figure 10 shows the comparison of the pressure dynamics occurring in all the spheres with a diameter of 2.5 mm. For every sphere the full grey-scale is given (on the left) and part of the grey scale, which is represented in the actual shadow beam (on the right). In this way the dynamics of pressures forming the shadow beam is shown. The corresponding values for spheres of various sizes and types of materials are listed in Table 1.

It is interesting to note a difference in acoustic pressure dynamics of gaseous spheres reaching the value of 15 dB when compared with all the other spheres (see Fig. 10). This observation is independent of the size of the sphere.

It is interesting to note that our approach is consistent with and in fact is a generalization of the simpler existing descriptions utilizing geometric (ray) acoustics of reflection and refraction when a circular structure is placed within an ultrasonic beam.

We present grey-scale shadow images of two cysts causing a convergent refraction (CR) and divergent refraction (DR) in Fig. 11. The convergent cyst shows a great increase of the acoustic pressure (bright patch) on the shadow axis near to the sphere surface while the divergent cyst has many additional bright side lobes of the main shadow due to the wave reflection and refraction on the cyst surface. The two images are in agreement with the computer-generated description of the paths of ultrasonic rays presented by Ziskin et al. (1990).

One should note that the shadow images obtained show an ideal case of visualization. In a real B-scan type of image the amplitude of returning echoes is more complicated. In our case, it was assumed that the echo amplitude is proportional to the incident *in situ* pressure. In practice, it depends also on the intrinsic echogenicity of acoustic discontinuities in the backward path of the echoes.

ACOUSTIC ISOBARS

Acoustic isobars, curves of constant acoustic pressure, are suitable for quantitative purposes. Figure 12 shows, as an example, isobars behind gaseous and kidney stone spheres with a radius of 2.5 mm ($f = 5$ MHz, $ka = 16.7\pi$). The numbers at the curves should be multiplied by 2 to obtain, in decibels, the level change in relation to the incident wave level (corresponding to 0 dB). To facilitate the readings of decibel numbers at isobars the figure was enlarged horizontally (by 2.6 times), though it causes some deformations of the isobar pattern.

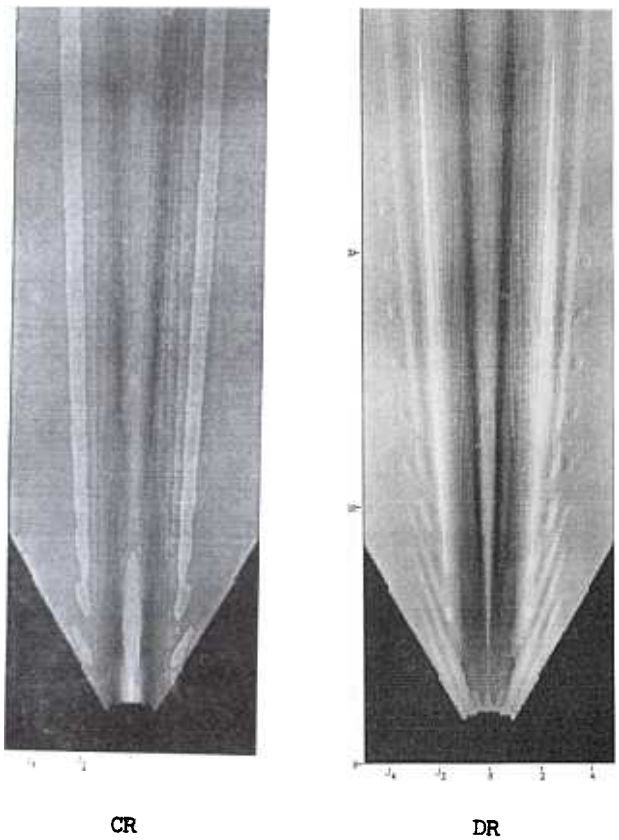

Fig. 11. Computed grey-scale images of spherical cysts causing a convergent refraction (CR) (wave speed in the cyst: 1300 m/s; in the surrounding tissue: 1500 m/s) and causing a divergent refraction (DR) (wave speed in the cyst: 1700 m/s). Spherical cyst radius $a = 2.5$ mm, $f = 5$ MHz, $ka = 16.7\pi$.

In previous articles, the first two authors (Filipczyński and Kujawska 1989; Filipczyński et al. 1991) have derived the following formula for the shadow length behind a rigid sphere (for the ka range 12–600)

$$r_{-6\text{dB}} = xa^2/\lambda \qquad (20)$$

where $r_{-6\text{dB}}$ is the length at which the pressure drop equals 6 dB in relation to the incident wave, λ is the wavelength, a is the sphere radius, and x is the proportionality factor for continuous wave (x_{cw}) equals 3.6.

Acoustic isobars corresponding to the 6-dB pressure drop, computed for all the spheres under consider-

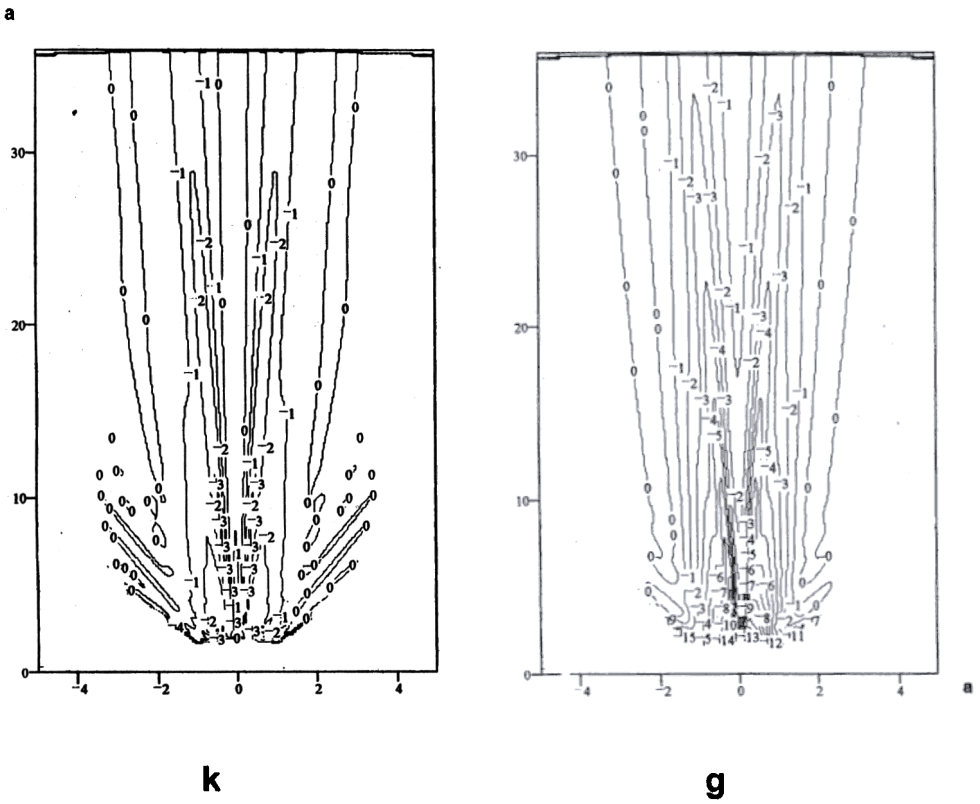

Fig. 12. Acoustic isobars computed for kidney stone (k) and gaseous (g) spheres (a = 2.5 mm, f = 5 MHz, ka = 16.7π). The numbers at the isobars should be multiplied by 2.

ation, allowed us to find directly the shadow length in every case. The results are collected in Table 2. In the two last columns the value of the proportionality coefficient, x, is shown. It is interesting to note that the coefficients are near to the previous value of x_{cw}. The value of x calculated for all the spheres independently of the sphere radius and sphere material equals 3.7 (with standard deviation 0.5). It means that for a rough estimation of the shadow length this value can be used giving an estimation error of about 20%.

CONCLUSIONS

The mathematical and numerical procedures presented can be used for obtaining shadow patterns behind spherical objects of various materials when using short pulses similar to those used in ultrasonography.

However, there are some limitations connected with ka values. For low values, such as those used in this study (not higher than 23.3π), a PC computer may be used; however, for higher values, such as those used in our previous study where ka was equal to 600 (Filipczyński and Kujawska 1989; Filipczyński et al. 1991), much more powerful computers should be used.

Due to this limitation, only spheres with a maximum radius of 3.5 mm at the frequency of 5 MHz were considered in our study. This seems to cover cases of some pathological structures like calcifications, small kidney or gall stones, and gaseous bubbles. The shadows behind rigid, steel, gaseous spheres, and spheres made of kidney stones were presented in an axonometric projection, in grey-scale as well as acoustic isobar patterns, showing many characteristic differences. One obtains a deep insight into the formation of the shadow showing its wave structure.

At the current state of this study two characteristic quantitative conclusions could be drawn. First, gaseous inclusions cause shadows with very high dynamics of acoustic pressures (about 15 dB higher in relation to

Table 2. Shadow length (r_{-6dB}) for various spheres

	a =			Value of x = $r_{-6dB}\lambda/a^2$	
Type of sphere	1 mm	2.5 mm	3.5 mm	Mean	SD
	12.0a	29.9a	41.8a	3.6	0.01
	10.5a	27.5a	38.5a	3.2	0.1
	14.6a	29.0a	39.8a	3.8	0.5
	14.7a	33.5a	46.0a	4.1	0.2

all the other spheres). Second, the shadow length—determined as the distance at which one observes a 6-dB drop of the acoustic pressure—followed the relation $r_{-6dB} = 3.7a^2/\lambda$ with the accuracy of about 20%, independently on the material or size of the sphere.

These two quantitative conclusions show that some possibilities of differentiating between gaseous and solid inclusions and of estimating the inclusion size from the shadow length exist. The question of whether and if what kind of information describing the spherical object can be additionally obtained from the shadow structure is a fundamental one and needs more study.

All our considerations were carried out for water as a tissuelike medium. However, in reality, one should first take into account the frequency-dependent tissue attenuation, which may change the results obtained for water to a great extent. The authors hope to present such an approach soon.

Acknowledgement—The authors thank the Committee of Scientific Research, Warsaw, for financial grant support.

REFERENCES

Anson L, Chivers R, Stockdale H. The calculation of Y_p for suspended sphere radiometer targets. Acustica 1981;48:302–307.

Beissner K. Maximum hydrophone size in ultrasound field measurements. Acustica 1985;59:61–66.

Bronsrtejn J, Semendjajew K. Sprawocznik po matematike. Moskwa: Nauka, 1967.

Dieulesaint E, Royer D. Ondes elastiques dans les solides. Paris: Masson et Cie, 1974.

Filipczyński L, Kujawska T. Acoustic shadow of a sphere immersed in water. I and II. Arch. Acoust. 1989;14:29–43, 181–190.

Filipczyński L, Kujawska T, Waszczuk T. The shadow behind a sphere immersed in water—measured, estimated and computed. IEEE Transac Ultrason Ferroelec Freq Control 1991;38:35–39.

Filipczyński L, Pawlowski Z, Wehr J. Ultrasonic methods of testing materials. London: Butterworth, 1966.

Hasegawa T, Kitagawa Y, Watanabe Y. Sound reflection from an absorbing sphere. J Acoust Soc Am 1977;62:1298–1300.

Kowalski H. The role of the shadow in the clinical practice. Private communication, Warsaw, 1994.

Morse O, Ingard K. Theoretical acoustics. New York: McGraw Hill, 1968.

Robinson, D, Wilson L, Kossoff G. Shadowing and enhancement in echograms by reflection and refraction. J Clin Ultrasound 1981;9:181–188.

Rzhevkin S. Kurs lekcyj po teorii zwuka. Iz d atestwo Moskowskowo Universiteta, 1960.

Rudgers, A. Acoustic pulses scattered by a rigid sphere immersed in a fluid. J Acoust Soc Am 1969;45:900–910.

Soetano K, Reid J. Regions in the B-mode image of a cylinder where the location of a point reflectoris changed by sound speed variations. Ultrasound Med Biol 1991;17:355–366.

Singh V, Agarwal R. Mechanical and ultrasound parameters of kidney stones. J Lithotripy Stone Dis 1990;2:117–123.

Ziskin M, LaFollette P, Blathras K, Varkey A. Effect of scan formation on refraction artifacts. Ultrasound Med Biol 1990;16:183–191.

APPENDIX

The coefficient, c_m, equals (Hasegawa et al. 1977)

$$= -[F_m j_m(ka) - ka j'_m(ka)]/[F_m h_m^{(2)}(ka) - kah_m^{(2)\prime}(ka)] \quad \text{(A1)}$$

where j'_m, $h_m^{(2)\prime}$ denote derivatives of Bessel and Hankel (second kind) spherical functions. F_m can be expressed by means of the formula (Anson et al. 1981):

$$F_m = x_2^2\rho(A_m \quad B_m)/2\rho_s(D_m - E_m) \quad \text{(A2)}$$

where:

$$A_m = [mj_m(x_1) - x_1 j_{m+1}(x_1)]/[(m-1)j_m(x_1) - x_1 j_{m+1}(x_1)] \quad \text{(A3)}$$

$$B_m = [2m(m+1)j_m(x_2)]/[(2m^2 - x_2^2 - 2)j_m(x_2) + 2x_2 j_{m+1}(x_2)] \quad \text{(A4)}$$

$$D_m = \{[x_2^2/2 - m(m \quad 1)]j_m(x_1) - 2x_1 j_{m+1}(x_1)\}: [(m-1)j_m(x_1) - x_1 j_{m+1}(x_1)] \quad \text{(A5)}$$

$$E_m = \{2m(m+1)[(1-m)j_m(x_2) + x_2 j_{m+1}(x_2)]\}: [(2m^2 - x_2^2 - 2)j_m(x_2) + 2x_2 j_{m+1}(x_2)] \quad \text{(A6)}$$

$$x_1 = cx/c_1 \quad \text{and} \quad x_2 = cx/c_2 \quad \text{(A7a,b)}$$

where c_1 and c_2 denote the longitudinal and transverse wave speeds, respectively.

For the rigid sphere $c_1 \to \infty$ and $c_2 \to \infty$. In such a case one obtains, from Eqn (A2), the value $F_m = 0$ and Eqn (A1) gives the coefficient c_m as expressed by Eqn (16).

For a gaseous sphere $\rho_s \cong 0$ and the value $F_m = \infty$ since $x_1 \neq 0$, $x_2 \neq 0$, $A_m \neq B_m$, $D_m \neq \infty$ and $E_m \neq \infty$. Then, Eqn (A1) gives the coefficient c_m as expressed by Eqn (17).